

Proposal for a new zero degree photon detector at BESIII

T. Hu^a, Y. F. Wang^a

R. Baldini^{b,c}, M. Bertani^b, S. Pacetti^{b,c}, A. Zallo^b,

M. Destefanis^d, M. Greco^d, M. Maggiora^d, S. Spataro^d

^a*Institute of High Energy Physics, Beijing, People's Republic of China*

^b*INFN, Laboratori Nazionali di Frascati, Frascati, Italy*

^c*Museo Storico della Fisica e Centro Studi e Ricerche "E. Fermi", Rome, Italy*

^d*Department of General Physics "A. Avogadro", University of Turin, Italy and INFN,
Turin, Italy*

ABSTRACT: A brand new design for the ZDD.

Contents

1. Design	1
1.1 Bremsstrahlung cross section	3
1.2 ISR cross section	5
2. Detector	6
2.1 The LYSO option	6
2.2 The lead-scintillating fiber option	7
3. Physics: $e^+e^- \rightarrow n\bar{n}\gamma_{\text{IS}}$	8
3.1 The $e^+e^- \rightarrow n\bar{n}\pi^0$ case	9
3.2 The $e^+e^- \rightarrow n\bar{n}\pi^0\gamma_{\text{IS}}$ case	11
4. The energy resolution	11
4.1 Energy slices in M_{had}	12
4.2 The $\bar{n}\gamma_{\text{IS}}$ missing mass	16
5. Including π^0	18
5.1 Energy slices in M_{had}	18
5.2 The $\bar{n}\gamma_{\text{IS}}$ missing mass with π^0 contamination	22
6. Radiation hardness	24

1. Design

The zero-degree detector (ZDD) is made of two identical stations, ZDD_F and ZDD_B in the forward and backward direction, located along the ideal z -axis, i.e. the beam direction in the e^+e^- center of mass frame (CoM), see fig. 1.

We are interested in the production of hadronic final states H through the so-called initial state radiation mechanism (ISR), i.e. the annihilation process $e^+e^- \rightarrow H\gamma_{\text{IS}}$, where the initial state (IS) photon γ_{IS} is emitted by one of the colliding leptons. The angular distribution of the ISR, see fig. 2, is peaked at small values of the scattering angle $\theta_{\gamma_{\text{IS}}}$, this makes the ISR acceptance of the ZDD (few mrad around $\theta_{\gamma_{\text{IS}}} = 0$ and $\theta_{\gamma_{\text{IS}}} = 180^\circ$) compatible with the wide angle acceptance in the whole BESIII volume ($20^\circ \leq \theta_{\gamma_{\text{IS}}} \leq 160^\circ$).

However, besides the ISR events, the small angle region is dominated by Bremsstrahlung photons produced in the process $e^+e^- \rightarrow e^+e^-\gamma$, which represent a severe background.

In fact, the ZDD design is dictated by the need to suppress such a Bremsstrahlung background. The almost totality of photons produced in $e^+e^- \rightarrow e^+e^-\gamma$ are emitted at very

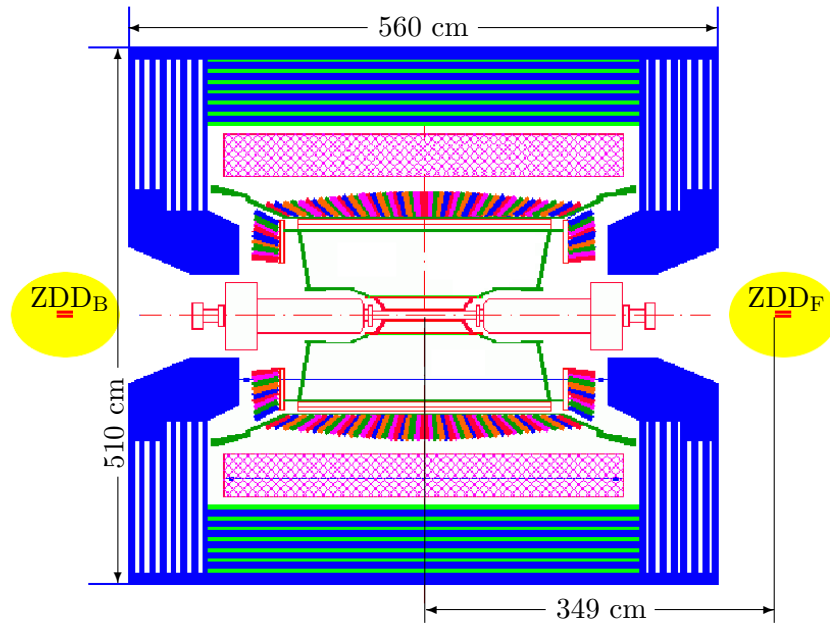


Figure 1: Overview of BESIII with ZDD detector installed. The ZDD stations are shown in red, highlighted by yellow ovals. All components are reported in scale.

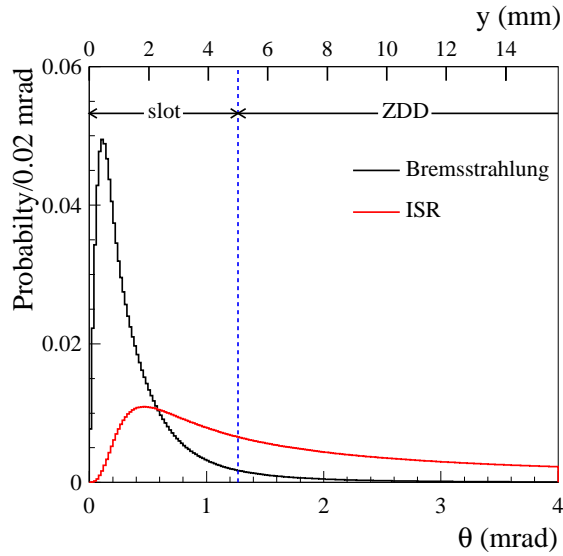


Figure 2: Angular distributions for emitted photons in Bremsstrahlung (black histogram) and ISR (red histogram) processes. The vertical dashed line indicates the slot (see text).

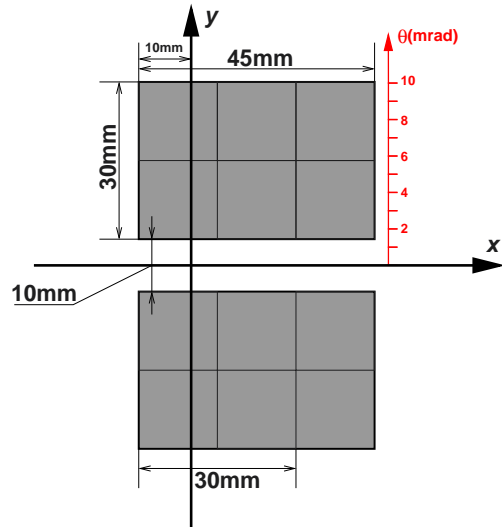


Figure 3: Front view of the ZDD detector. The central 10 mm wide region represents the Bremsstrahlung slot.

small angles. The corresponding angular distribution, shown in fig. 2 as a black histogram, is more peaked than the ISR one, red histogram.

This fact makes possible a geometrical separation of the two effects. A 10 mm wide slot in the detector, along the x axis, between $y = -5$ mm and $y = +5$ mm (blue dashed line in fig 2) would drastically reduce the Bremsstrahlung contamination in ISR events.

Figure 3 shows the front view, x - y cross section, of the ZDD. It is split in two identical pieces with an empty horizontal region, that we call “slot”. Such a region collects more than the 97% of the Bremsstrahlung photons, i.e. the Bremsstrahlung contamination over the active surface of the ZDD is reduced by a factor of ~ 35 .

1.1 Bremsstrahlung cross section

We can estimate the total Bremsstrahlung cross section relying on the formulae given in Ref. [1]. The parameters we used are

$$E_{\text{cm}} = 2 \times 1.89 \text{ GeV} \quad E_{\gamma}^{\text{min}} = 50 \text{ MeV},$$

while the maximum photon energy is

$$E_{\gamma}^{\text{max}} = \frac{E_{\text{cm}}}{2} \left(1 - \frac{4m^2}{E_{\text{cm}}^2} \right),$$

where m is the electron mass.

The total Bremsstrahlung cross section, over the whole 4π solid angle, is

$$\sigma_{\text{Bre}}(4\pi) \equiv \int_{4\pi} \frac{d\sigma_{\text{Bre}}}{d\Omega} d\Omega \simeq 352.6 \text{ mb},$$

where the subscript “Bre” stands for Bremsstrahlung. As a consequence of the extremely peaked angular distribution, see fig. 2, we find that **more than 99.4% of the photons end up in the ZDD+slot area**, indeed the corresponding cross section is

$$\sigma_{\text{Bre}}(\text{ZDD} + \text{slot}) \equiv \int_{\text{ZDD}+\text{slot}} \frac{d\sigma_{\text{Bre}}}{d\Omega} d\Omega \simeq \underbrace{10.5 \text{ mb}}_{\sigma_{\text{Bre}}(\text{ZDD})} + \underbrace{340.0 \text{ mb}}_{\sigma_{\text{Bre}}(\text{slot})} = 350.5 \text{ mb}. \quad (1.1)$$

The slot reduces the Bremsstrahlung cross section from 350.5 mb to only 10.5 mb, i.e. less than 3%.

The slot and ZDD cross sections, given in eq. (1.1), account also for the angular beam spreading. In particular we consider the spreading in the x and y directions separately as

$$\Delta\theta_{x,y} = \sqrt{\frac{\epsilon_{x,y}}{\beta_{x,y}^*}}, \quad (1.2)$$

where $\epsilon_{x(y)}$ and $\beta_{x(y)}^*$ are the $x(y)$ emittance and betatron amplitude. Using the BEPCII values [3]

$$\begin{aligned} \epsilon_x &= 144 \times 10^{-9} \text{ m} & \beta_x^* &= 1 \text{ m} \\ \epsilon_y &= 2.2 \times 10^{-9} \text{ m} & \beta_y^* &= 0.015 \text{ m}, \end{aligned} \quad (1.3)$$

we get angular and linear spreading as

$$\Delta\theta_x = \Delta\theta_y = 0.38 \text{ mrad} \quad \Rightarrow \quad \Delta x = \Delta y = R \cdot \Delta\theta_x, \quad (1.4)$$

$R = 349$ cm is the distance from the interaction point to the ZDD, see fig. 1. Finally, the beam spreading effect in the ZDD-Bremsstrahlung cross section has been included in the computation using this formula

$$\sigma_{\text{Bre}}(\text{ZDD}) = \frac{2}{2\pi\Delta x\Delta y} \cdot \int dx dy \int_{I_x} dx' \int_{I_y} dy' \frac{d\sigma_{\text{Bre}}}{d\Omega}(x, y) \left| \frac{\partial(\theta, \phi)}{\partial(x, y)} \right| e^{-\frac{(x-x')^2}{2\Delta x^2}} e^{-\frac{(y-y')^2}{2\Delta y^2}}, \quad (1.5)$$

where the initial factor of two accounts for the forward and backward parts of the ZDD, $\left| \frac{\partial(\theta, \phi)}{\partial(x, y)} \right|$ is the Jacobian determinant and, the x and y integration intervals are

$$I_x = [-10 \text{ mm}, 35 \text{ mm}], \quad I_y = [-35 \text{ mm}, -5 \text{ mm}] \cup [5 \text{ mm}, 35 \text{ mm}]. \quad (1.6)$$

For a single ZDD station, assuming the peak luminosity: $\mathcal{L} = 0.8 \cdot 10^{33} \text{ cm}^{-2}\text{s}^{-1}$, the Bremsstrahlung rate is

$$\frac{1}{2} \sigma_{\text{Bre}}(\text{ZDD}) \times \mathcal{L} = (5.3 \cdot 10^{-3} \cdot 10^{-24} \text{ cm}^{-2}) \times (0.8 \cdot 10^{33} \text{ cm}^{-2}\text{s}^{-1}) = \mathbf{4.2 \text{ MHz}}. \quad (1.7)$$

This rate can be further reduced by a factor of two using the additional fragmentation of the ZDD in upper and lower part.

We can consider the expected Bremsstrahlung rate at different photon energies or integrating from various lower limits for E_γ .

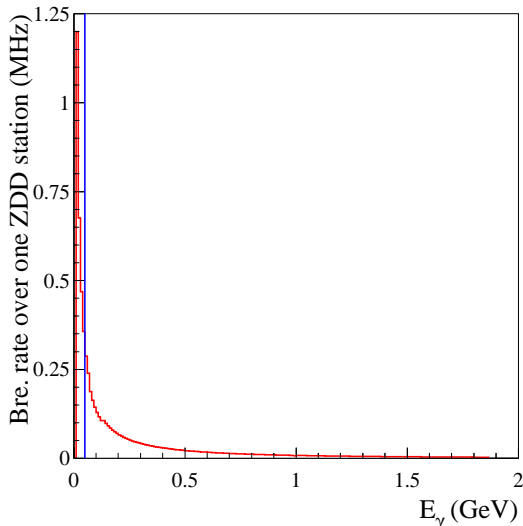


Figure 4: Bremsstrahlung rate in 10 MeV intervals of the photon energy E_γ . The blue vertical line highlights the 50 MeV lower limit used in our study.

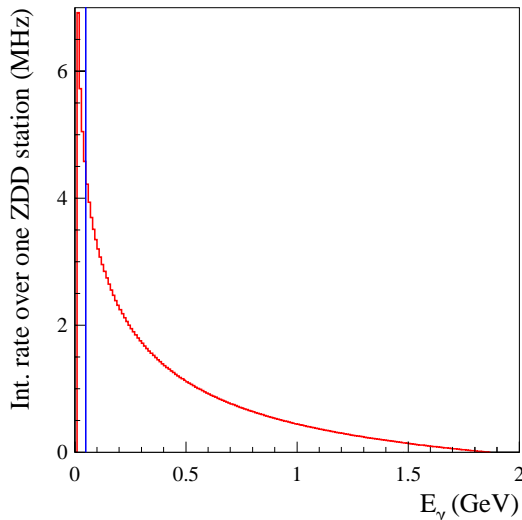


Figure 5: Integrated Bremsstrahlung rate as a function of the minimum value of E_γ . The blue vertical line highlights the 50 MeV lower limit used in our study.

Figure 4 shows, in 10 MeV bins, the expected Bremsstrahlung rate in one ZDD station, while fig. 5 represents its integral, i.e. at each energy E_γ we report

$$\int_{E_\gamma}^{E_\gamma^{\text{max}}} \frac{d\sigma_{\text{Bre}}}{dE'_\gamma} dE'_\gamma. \quad (1.8)$$

For instance the first bin after the 50 MeV threshold (blue line) in fig. 5 corresponds the total rate obtained in eq. (1.7).

1.2 ISR cross section

Thanks to a mild angular behavior, see fig. 2, the ISR cross section is affected by a smaller reduction as a consequence of the slot. More in detail, the ISR contributions of ZDD and slot are

$$\frac{\sigma_{\text{ISR}}(\text{ZDD})}{\sigma_{\text{ISR}}(4\pi)} = 13.7\% \quad \frac{\sigma_{\text{ISR}}(\text{slot})}{\sigma_{\text{ISR}}(4\pi)} = 19.6\%. \quad (1.9)$$

This ISR luminosity for the ZDD is similar to that of *BABAR* at wide angle. We considered also other possible positions of the ZDD. Table 1 reports results for ratios and Bremsstrahlung cross sections obtained with three possible values of x_{min} , i.e. the left side coordinate of the ZDD. By shifting the ZDD on the right, see fig. 3, the geometrical acceptance and corresponding cross sections decrease for both Bremsstrahlung and ISR events.

x_{min} (mm)	$\frac{\sigma_{\text{B}}(\text{ZDD})}{\sigma_{\text{B}}(\text{ZDD} + \text{slot})}$	$\frac{\sigma_{\text{B}}(\text{ZDD})}{\sigma_{\text{B}}(4\pi)}$	$\sigma_{\text{B}}(\text{ZDD})$ (mb)	$\frac{\sigma_{\text{ISR}}(\text{ZDD})}{\sigma_{\text{ISR}}(\text{ZDD} + \text{slot})}$	$\frac{\sigma_{\text{ISR}}(\text{ZDD})}{\sigma_{\text{ISR}}(4\pi)}$
-10	2.8%	2.8%	9.7	41.2%	13.7%
-5	2.5%	2.5%	8.8	40.0%	12.0%
0	2.9%	1.5%	5.2	46.8%	9.3%

Table 1: Ratios and Bremsstrahlung cross sections for different x positions of the detector.

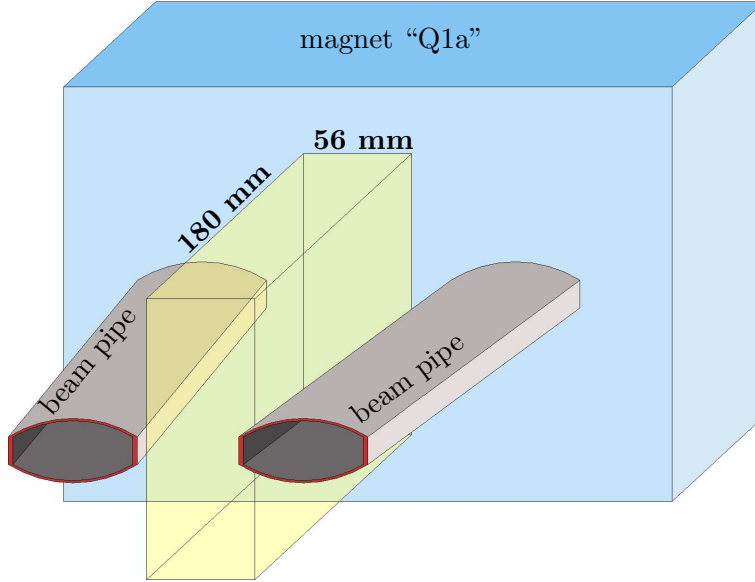


Figure 6: Schematic overview of the available space for the ZDD. The yellow shaded volume represents the maximal allowed occupancy.

2. Detector

The physical occupancy of the ZDD is primarily determined and constrained by the available space which is 180 mm long with a front width of 56 mm and rear width of 69 mm. In fig. 6 this volume is represented by a yellow parallelepiped of the maximum allowed length, 180 mm, and 56 mm width, concerning the height, apparently there are no stringent limitations. As a consequence of the narrowness of the available region, the design of the detector must be very compact.

For each of the two ZDD stations we propose the scheme shown in fig. 7. This structure fits into a volume of $45(w) \times 70(h) \times 160(l)$ mm³, hence there remain further 20 mm of length and at least 11 mm of width that can be used to install the readout electronics and possible motion mechanisms.

We considered two possible classes of detectors: a LYSO crystal calorimeter readout by APD photosensors and lead-scintillating fiber (Pb-Scint) calorimeter (à la KLOE) instrumented with multianode photomultipliers.

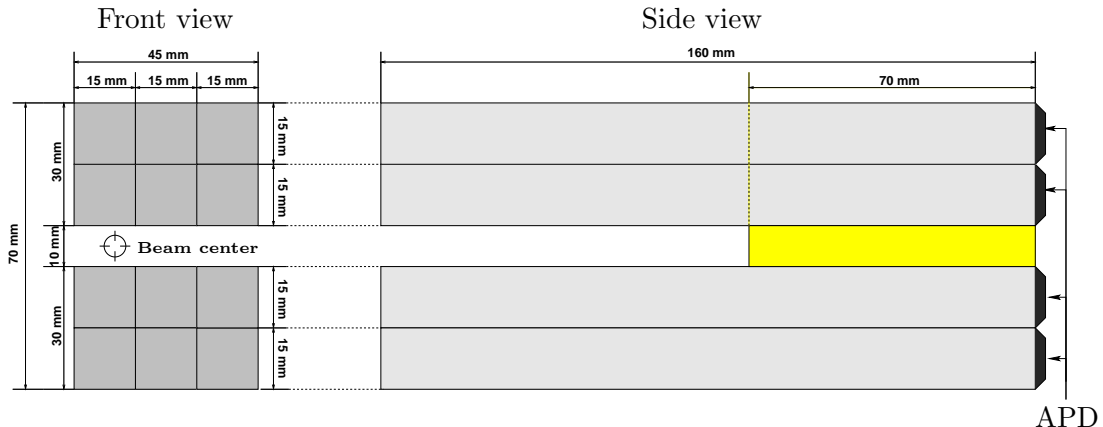


Figure 7: Front and side view of the zero degree detector. The gun sight, in the front view indicates the impact point of photon emitted exactly at zero degree. The yellow area shows the location of a possible additional Luminosity detector.

2.1 The LYSO option

Figure 7 shows a detailed design of one of the ZDD stations. It is made of two 2×3 arrays of $15 \times 15 \times 160$ mm³ barrels of LYSO crystals readout by APDs. There is also the possibility to introduce a calorimeter in between the two arrays to cover the very small angle region. We could use the last 70 mm of the slot, the yellow area in fig. 7, to install a “squeezed” version of the existing luminosity-detector [2].

The energy resolution of this calorimeter has been estimated using a GEANT4 simulation. As a consequence of its location, photons hit the ZDD almost perpendicularly. We have considered first two extreme cases for the geometry of the ZDD, i.e. we have illuminated a central and a corner test region of the upper element, these 5×5 mm² regions are shown as gray squares in fig. 8. Table 2 reports results for the energy resolution $\sigma_{E_\gamma}/E_\gamma$ in two

E_γ (GeV)	$\sigma_{E_\gamma}/E_\gamma$ central	$\sigma_{E_\gamma}/E_\gamma$ corner
1.0 - 1.4	3.6%	26.0%
0.2 - 0.4	4.9%	32.0%
0.2 - 1.4	4.1%	26.7%

Table 2: LYSO option: energy resolution for different energies and positions.

E_γ (GeV)	$\sigma_{E_\gamma}/E_\gamma$
1.0	7.9%
0.5	9.5%

Table 3: LYSO option: energy resolution for ISR photons.

energy intervals, first two rows, and over the whole range, last row. The energy resolution obtained by using the ISR density, shown in colors in fig. 8, is given in tab. 3.

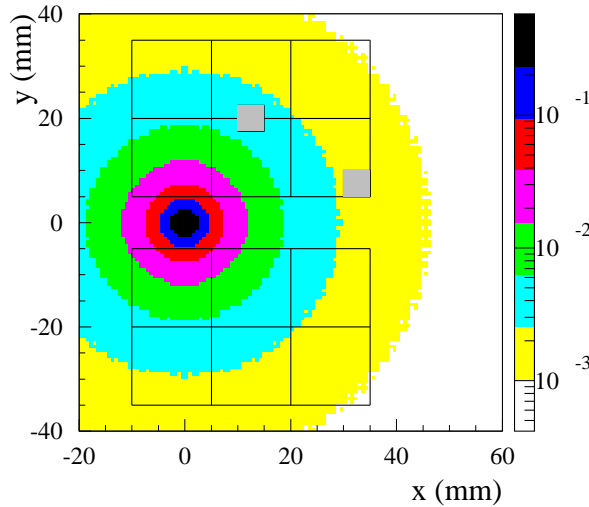


Figure 8: In colors the ISR distribution density over the ZDD cross section. The grey squares are the ZDD test regions.

2.2 The lead-scintillating fiber option

In the second option the ZDD is a lead-scintillating fibers calorimeter à la KLOE [4]. The external structure, shown in fig. 9, is the same as the one of previous LYSO case. Each station is made by two stacks, upper and lower, of about 320 grooved 0.5 mm thick lead foils (for a total length of 160 mm) along the z axis, alternated with layers of cladded 1 mm diameter scintillating fibers disposed along the y axis. The fibers are readout by photomultipliers (PM) disposed above the upper and below the lower element as shown in fig. 9.

Figure 10 shows a xz section of the calorimeter, the fibers are arranged in periodic equilateral triangle arrays whose side is 1.35 mm.

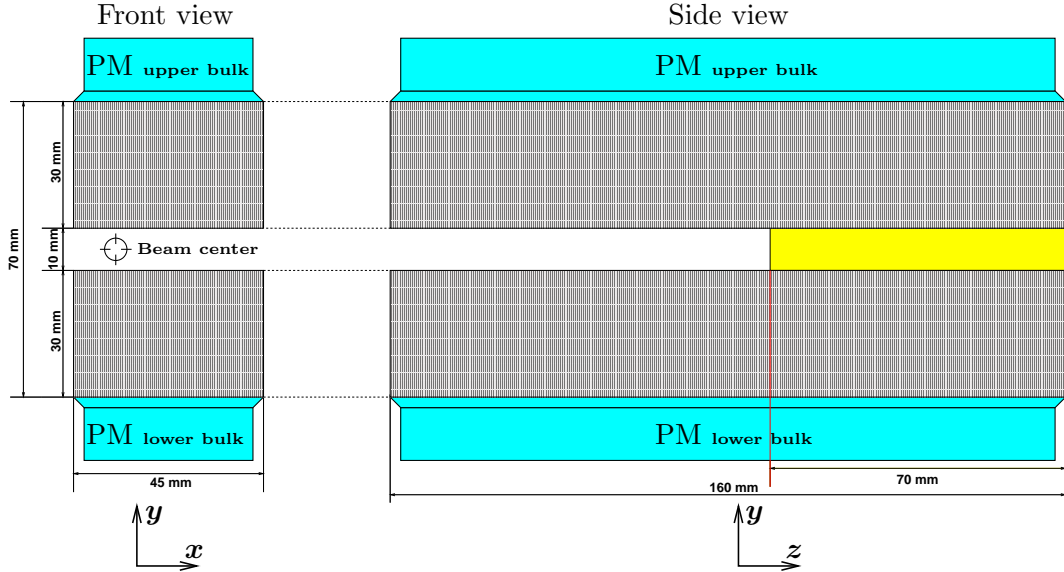


Figure 9: Front and side view of the ZDD in case of lead-scintillating fiber option. The gun sight, in the front view indicates the impact point of photon emitted exactly at zero degree. The pale blue devices are photomultiplier bulks. The yellow area shows the location of a possible additional Luminosity detector.

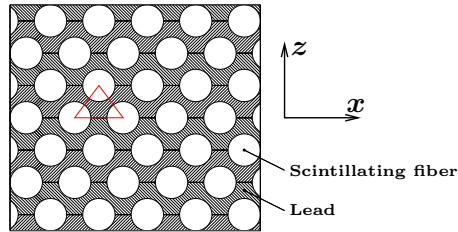


Figure 10: Lead-scintillating fibers structure. The diameter of scintillating fibers is 1 mm, they are arranged in a periodic equilateral triangle array, shown in red, whose side is 1.35 mm.

In this case the energy resolution for ISR photons, i.e. photons hitting the ZDD according to the angular distribution of fig. 8, is reported in tab. 4.

3. Physics: $e^+e^- \rightarrow n\bar{n}\gamma_{\text{ISR}}$

We are interested in using the ISR technique to measure baryon-antibaryon hadronic cross sections, i.e. cross sections of processes like $e^+e^- \rightarrow \mathcal{B}\bar{\mathcal{B}}\gamma_{\text{ISR}}$, where \mathcal{B} stands for a generic baryon. Interesting and pioneering results have been obtained in this field by the *BABAR* Collaboration [5, 6], that, for the first time, exploited such a technique to measure with

E_γ (GeV)	$\sigma_{E_\gamma}/E_\gamma$
1.0	20.3%
0.5	26.4%

Table 4: Lead-scintillating fibers option: energy resolution for ISR photons.

unprecedented accuracy cross sections for $p\bar{p}$, $\Lambda\bar{\Lambda}$, $\Lambda\bar{\Sigma}^0 + \text{c.c.}$, and $\Sigma^0\bar{\Sigma}^0$. Nevertheless the possibility of observing the $n\bar{n}$ final state in *BABAR* appears quite unlikely [7]. BESIII offers a unique opportunity to perform such a measurement thanks to its TOF system. Besides the accidental coincidences where a photon produced in the Bremsstrahlung process $e^+e^- \rightarrow e^+e^-\gamma$ mimics the ISR, that will be discussed later on, we consider two main sources of background:

- $e^+e^- \rightarrow n\bar{n}\pi^0$;
- $e^+e^- \rightarrow n\bar{n}\pi^0\gamma_{\text{ISR}}$.

3.1 The $e^+e^- \rightarrow n\bar{n}\pi^0$ case

Exploiting the ISR technique by tagging the initial photon at zero degrees instead of at wide angles, as it is done in *BABAR* and Belle for instance, strongly favors the suppression of the severe background represented by final states with a π^0 in place of γ_{ISR} .

Indeed, let us consider the process $e^+e^- \rightarrow H\pi^0$, with $\pi^0 \rightarrow \gamma\gamma$, there is the possibility that the lower energy photon escapes detection, in such a case the remaining photon would mimic the ISR process $e^+e^- \rightarrow H\gamma_{\text{ISR}}$.

To estimate the $n\bar{n}\pi^0$ background events we rely in the measurement of the $p\bar{p}$ cross section performed by the *BABAR* Collaboration using the wide-angles ISR technique [5]. We will exploit their evaluation of the $p\bar{p}\pi^0$ background, with π^0 at wide angles ($\cos(160^\circ) \leq \cos\theta_{\pi^0} \leq \cos(20^\circ)$), to estimate the expected $n\bar{n}\pi^0$ events.

The wide-angles ISR luminosity is usually expressed as a derivative w.r.t. the energy or momentum of the hadronic final state, in particular, considering a symmetric angular acceptance: $\theta_{\min} \leq \theta_\gamma \leq \theta_{\min} - \pi$, we have

$$\frac{dL}{dM_{n\bar{n}}} = \frac{2M_{n\bar{n}} L_{e^+e^-}}{E_{\text{cm}}^2} \frac{\alpha}{\pi x} (2 - 2x + x^2) \ln\left(\frac{1 + \cos\theta_{\min}}{1 - \cos\theta_{\min}}\right), \quad x = \frac{2E_\gamma}{E_{\text{cm}}}, \quad (3.1)$$

where $L_{e^+e^-}$ represents the instantaneous or integrated luminosity of the machine, x is the γ_{ISR} energy normalized to that of the beam, and $M_{n\bar{n}}$ is the invariant mass of the hadronic final state H , in our case: $H = n\bar{n}$. We can compute the gain factor of BESIII w.r.t. *BABAR* at $M_{n\bar{n}} = 2M_n$, i.e. at the hadronic threshold, as a function of the ratio between the total luminosities, i.e. the quantity

$$G(E_{\text{cm}}) = \frac{(dL/dM_{n\bar{n}})_{\text{BESIII}}/L_{e^+e^-}^{\text{BESIII}}}{(dL/dM_{n\bar{n}})_{\text{BABAR}}/L_{e^+e^-}^{\text{BABAR}}}, \quad (3.2)$$

which is represented in fig. 11 as a function of the CoM energy of BESIII. At the $\psi(3770)$ mass the gain factor is $G(M_{\psi(3770)}) = 10.7$.

In the *BABAR* case, the $p\bar{p}\pi^0$ production directly at the $\Upsilon(4S)$ mass represents only a negligible background for the process $e^+e^- \rightarrow p\bar{p}\gamma_{\text{IS}}$, in particular they found a ratio background-to-signal of about 6%. More in detail, at the $p\bar{p}$ threshold

$$R_{BABAR} = \frac{\text{Events}(p\bar{p}\pi^0)}{\text{Events}(p\bar{p}\gamma)} = \frac{L_{e^+e^-}^{BABAR} \cdot \sigma(e^+e^- \rightarrow p\bar{p}\pi^0)}{(dL/dM_{p\bar{p}}) \cdot \sigma(e^+e^- \rightarrow p\bar{p}\gamma_{\text{IS}})} (M_{\Upsilon(4S)}) = 0.06. \quad (3.3)$$

In BESIII at the $\psi(3770)$ mass, being

$$\frac{\sigma(e^+e^- \rightarrow p\bar{p}\pi^0) [M_{\Upsilon(4S)}]}{\sigma(e^+e^- \rightarrow p\bar{p}\pi^0) [M_{\psi(3770)}]} > \frac{3 \times 10^{-6} \text{ nb}}{0.012 \text{ nb}}, \quad (3.4)$$

(the inequality is due to the fact that we know only the upper limit for the cross section $\sigma(e^+e^- \rightarrow p\bar{p}\pi^0) [M_{\psi(3770)}]$) it follows that

$$\begin{aligned} R_{\text{BESIII}} &= \frac{\text{Ev}(p\bar{p}\pi^0)}{\text{Ev}(p\bar{p}\gamma)} = \frac{L_{e^+e^-} \cdot \sigma(e^+e^- \rightarrow p\bar{p}\pi^0)}{(dL/d\sqrt{s}) \cdot \sigma(e^+e^- \rightarrow p\bar{p}\gamma_{\text{IS}})} [M_{J/\psi}] \\ &< 0.06 \times \underbrace{\left(\frac{0.012}{3 \times 10^{-6}} \right)}_{p\bar{p}\pi^0 \text{ cross section ratio}} \times \underbrace{\left(\frac{1}{10.7} \right)}_{\text{Lum. ratio}} = 22.4, \end{aligned} \quad (3.5)$$

where we have used the results of eqs. (3.3) and (3.4). This large ratio background-to-signal makes very difficult to use the ISR at wide angles to measure the $p\bar{p}$ cross section at BESIII. The same argument can be used also for the $n\bar{n}$ cross section, indeed we expect similar cross sections for hadronic final states with neutrons in place of protons, i.e. for instance

$$\sigma(e^+e^- \rightarrow n\bar{n}\pi^0) [M_{J/\psi}] \simeq \sigma(e^+e^- \rightarrow p\bar{p}\pi^0) [M_{J/\psi}].$$

The zero-degrees ISR technique, instead, does not have this limitation. The $n\bar{n}\pi^0$ cross section at the $\psi(3770)$ mass over the ZDD surface can be obtained assuming a flat angular distribution for π^0 and scaling the total cross section by the ratio between the ZDD and BESIII detector solid angles

$$\frac{2 \times (2 \cdot 4.5 \cdot 3/349^2)}{\int_{-\cos\theta_{\min}}^{+\cos\theta_{\min}} d\cos\theta \int_0^{2\pi} d\phi} = \frac{4.4 \times 10^{-4}}{2\pi \cos\theta_{\min}} = 7.5 \times 10^{-5}, \quad (3.6)$$

where the first factor of two at numerator accounts for the forward and backward ZDD, while the second is for the upper and lower elements. In light of this result, the ratio of eq. (3.5), with π^0 photons at zero degrees, becomes

$$R_{\text{BESIII}}(\gamma_{\pi^0} \rightarrow 0^\circ) = 0.0017, \quad (3.7)$$

and it is completely negligible.

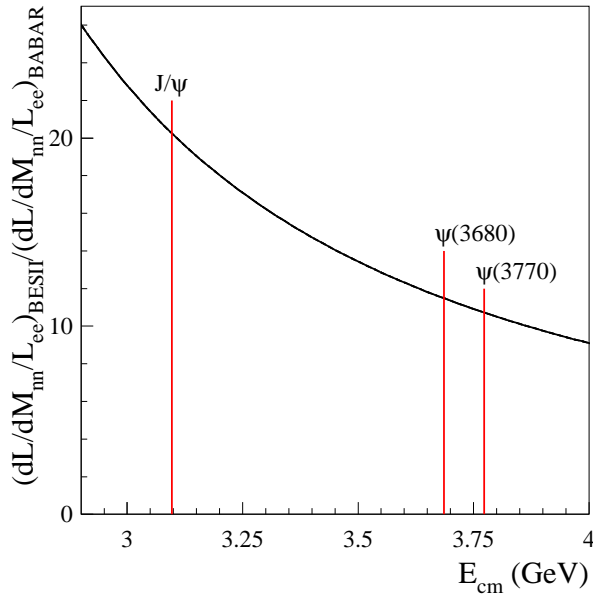


Figure 11: BESIII vs. *BABAR* gain factor evaluated at the hadronic threshold $M_{n\bar{n}} = 2M_n$ as a function of the BESIII CoM energy E_{cm} . The vertical red lines highlight the ψ resonances.

3.2 The $e^+e^- \rightarrow n\bar{n}\pi^0\gamma_{\text{IS}}$ case

The ISR process $e^+e^- \rightarrow n\bar{n}\pi^0\gamma_{\text{IS}}$ represents an important background indeed, when the π^0 remains undetected, it has the same signature of the signal. To reduce such a background we relay first in the BESIII efficiency in detecting π^0 's and second, for those events where π^0 photons escape detection, we use the kinematic fit procedure (KF).

More in detail, we consider as background those events where at least one of the π^0 photons is lost, i.e.:

- it hits the detector in a 200 mrad cone around the \bar{n} direction;
- it is out of the geometrical acceptance;

and the remaining photon has an energy less than 50 MeV. In all other cases, either the π^0 or an hard photon is detected and hence the event is rejected.

The process $e^+e^- \rightarrow n\bar{n}\pi^0\gamma_{\text{IS}}$ has been simulated using the *BABAR* result of Ref. [5], and assuming for BESIII a ratio between the $n\bar{n}$ and $n\bar{n}\pi^0$ efficiencies similar to that of *BABAR*. The yields of the considered cross sections are shown in fig. 12.

4. The energy resolution

10000 events $e^+e^- \rightarrow n\bar{n}\gamma_{\text{IS}}$ have been generated with the following properties

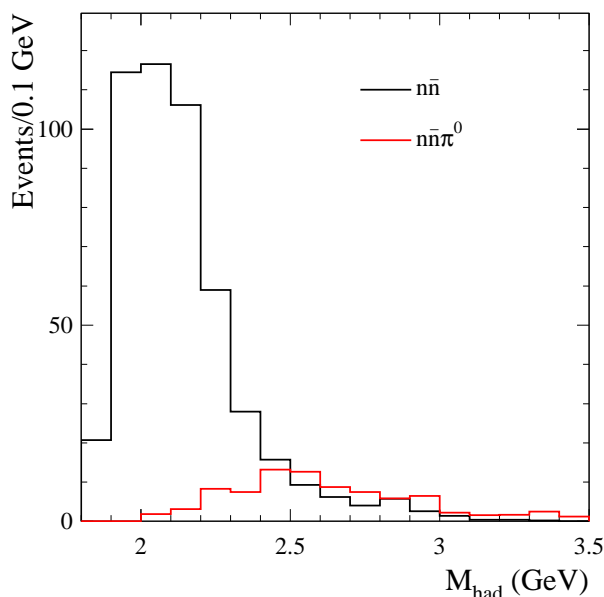


Figure 12: Yields for $e^+e^- \rightarrow n\bar{n}\gamma_{\text{IS}}$ and $n\bar{n}\pi^0\gamma_{\text{IS}}$ cross sections [5].

- center of mass energy $E_{\text{cm}} = 3.77 \text{ GeV}$;
- photon energy $0.16 \text{ GeV} \leq E_{\gamma_{\text{IS}}} \leq \frac{E_{\text{cm}}}{2} \left(1 - \frac{4M_n^2}{E_{\text{cm}}^2}\right)$;
- photon scattering angle $\theta_{\gamma_{\text{IS}}} \leq 3 \text{ mrad}$.

Figure 13 shows how the $n\bar{n}$ invariant mass distribution changes as a consequence of the geometrical cut first, and then the kinematical fit (KF). The geometrical acceptance of the BESIII detector is

- $\theta \in [35^\circ, 145^\circ]$ for the barrel;
- $\theta \in [18^\circ, 32^\circ] \cup [148^\circ, 162^\circ]$ for the endcaps.

The geometrical cut corresponds to the requirement that the antineutron is produced within this acceptance. The KF instead, is performed assuming that only the IS photon and the antineutron are detected. If we consider only events with KF- χ^2 below 10, see fig. 14, we get the $n\bar{n}$ distribution shown as a black histogram in fig. 13. In other words, almost all the events ($\sim 99\%$) which have passed the geometrical cut survive to the KF procedure.

4.1 Energy slices in M_{had}

We consider seven values of the hadronic invariant mass M_{had} , from 2.0 up to 3.2 GeV in steps of 0.2 GeV. More in detail, M_{had} is defined as

$$M_{\text{had}} = \sqrt{(q - p_{\gamma_{\text{IS}}})^2} = E_{\text{cm}} \sqrt{1 - 2E_{\gamma_{\text{IS}}}/E_{\text{cm}}}, \quad (4.1)$$

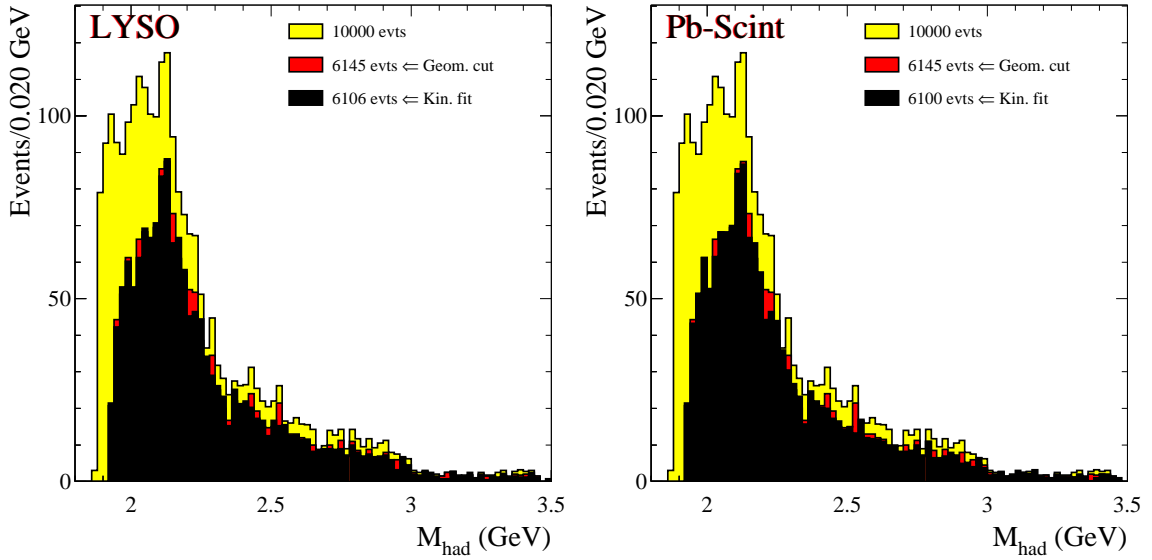


Figure 13: The yellow histogram shows the generated $n\bar{n}$ invariant mass distribution that corresponds to 10000 events. This number reduces to 6145 when the geometrical cut is applied and, finally to 6106 in case of LYSO (left) and 6096 in case of Pb-Scint (right) after the kinematical fit. See text for details.

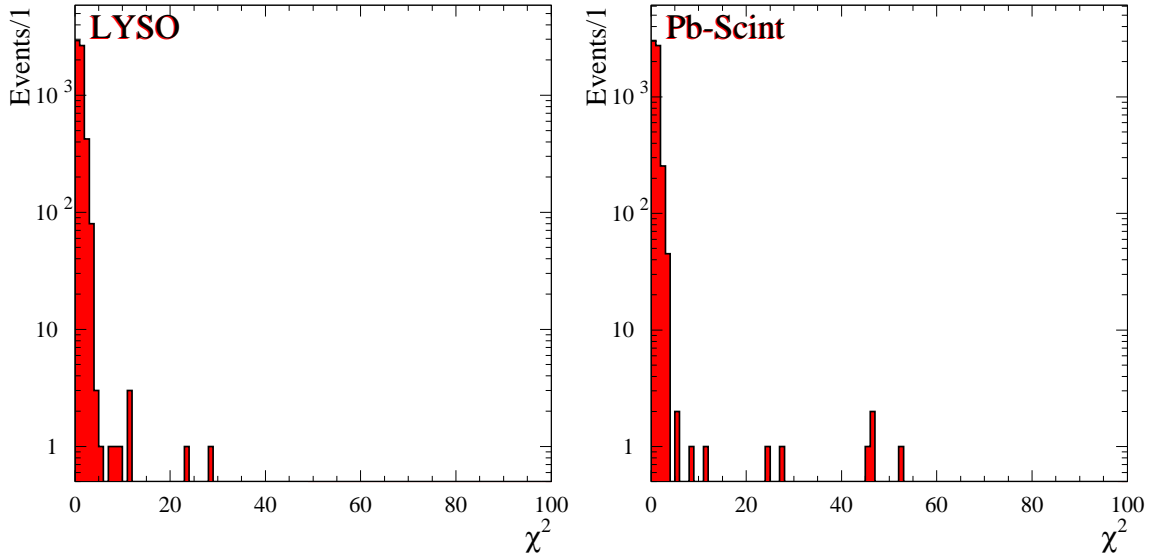


Figure 14: χ^2 distribution for $e^+e^- \rightarrow n\bar{n}\gamma_{1S}$ events, where only γ_{1S} and \bar{n} are detected. LYSO on the left and Pb-Scint on the right.

where $q = (E_{\text{cm}}, 0, 0, 0)$ is the total CoM 4-momentum of the initial e^+e^- pair.

Figures 15 and 16 show the M_{had} energies reconstructed with the KF procedure.

Figure 17 shows the obtained energy resolution in both cases, LYSO and Pb-Scint. The resolution improvement as M_{had} decreases is due the dominance of the ZDD energy reso-

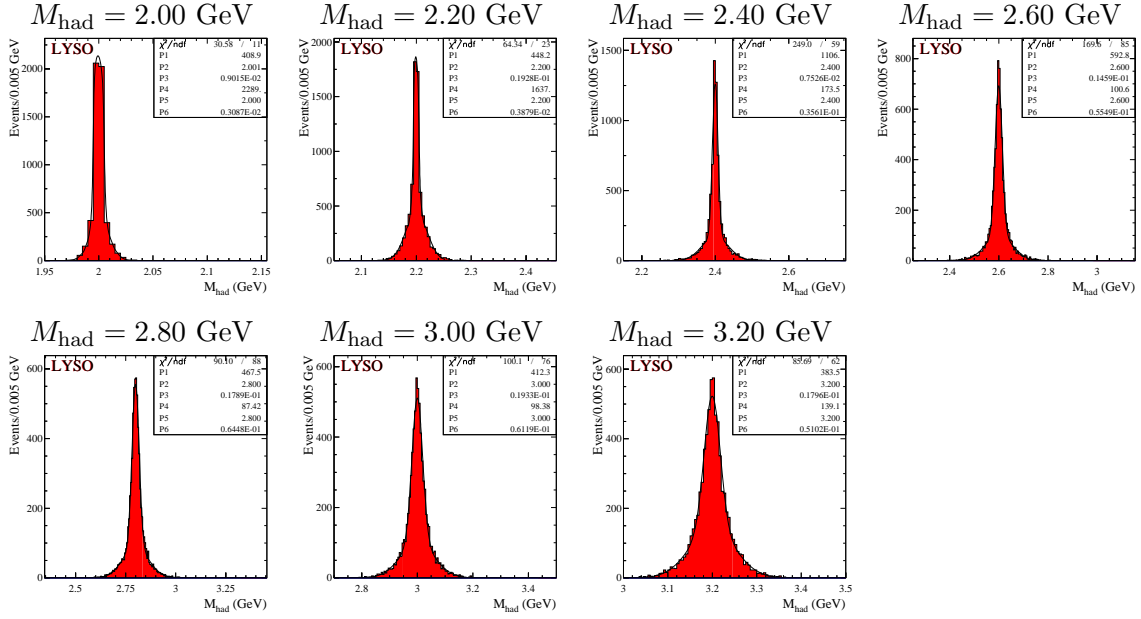


Figure 15: Energy distributions obtained in the case of LYSO detector. The curves are the fits.

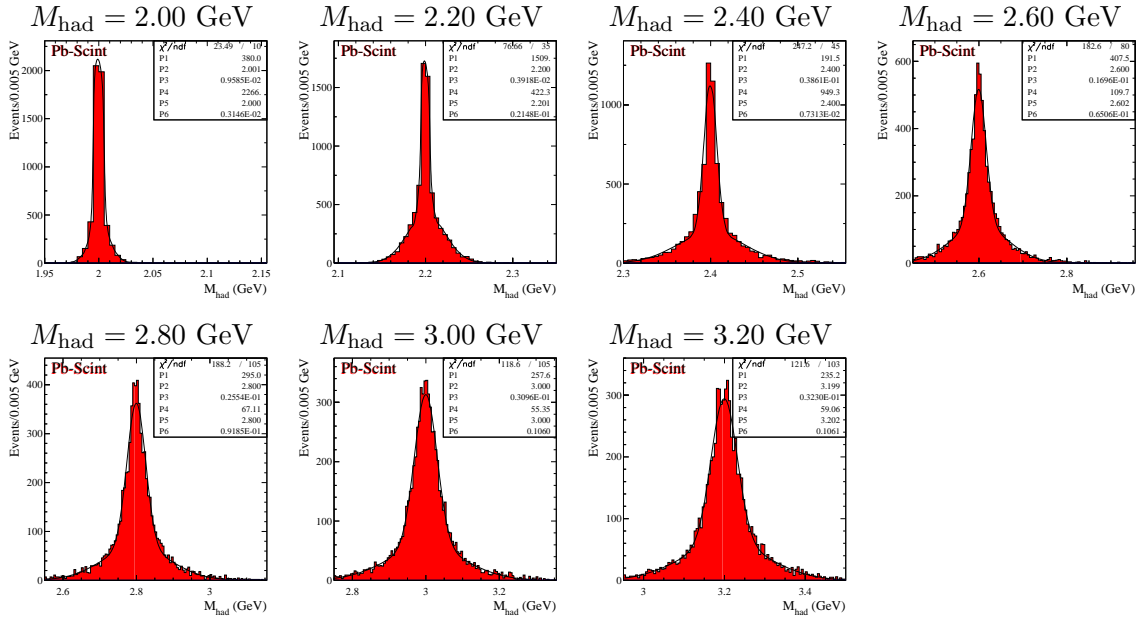


Figure 16: Energy distributions obtained in the case of Pb-Scint detector. The curves are the fits.

lution for the ISR photon. Indeed, following eq. (4.1), lower values of M_{had} correspond to higher values of $E_{\gamma_{\text{ISR}}}$.

Finally, fig. 18 shows the percentage of events which survives to the geometrical and χ^2 cuts. More in detail the geometrical cut corresponds to require that **only** \bar{n} ends up in

BESIII. This means that it has to be produced with scattering angle θ_2 such that

$$\underbrace{|\cos \theta_2| \leq \cos(35^\circ)}_{\text{barrel}} \quad \text{or} \quad \underbrace{\cos(32^\circ) \leq |\cos \theta_2| \leq \cos(18^\circ)}_{\text{endcaps}}. \quad (4.2)$$

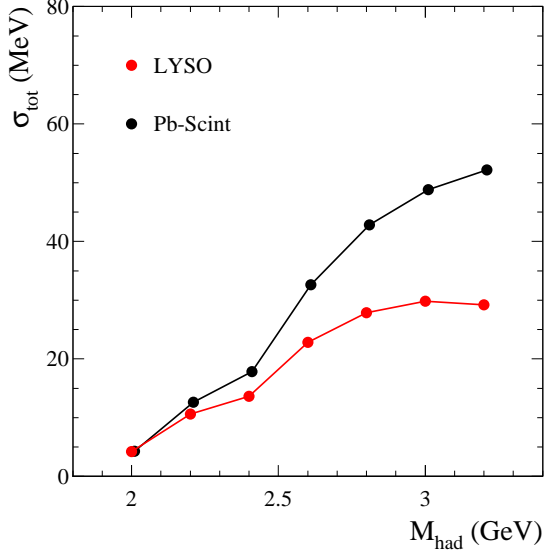


Figure 17: Energy resolution in the $n\bar{n}$ invariant mass for the LYSO (red) and Pb-Scint (black) case.

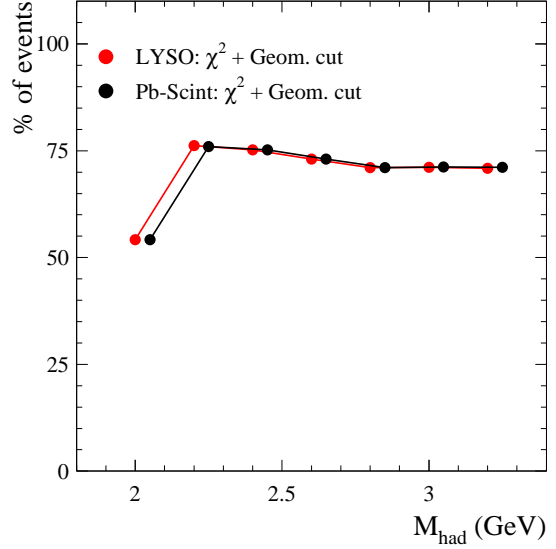


Figure 18: Percentage of events surviving to the χ^2 and geometrical cuts, i.e.: \bar{n} in BESIII and $\text{KF-}\chi^2 < 10$.

The $\text{KF-}\chi^2$ cut corresponds to

$$0 < \chi^2 < 10, \quad (4.3)$$

but, as can be seen in fig. 14, such a cut is widely fulfilled.

4.2 The $\bar{n}\gamma_{IS}$ missing mass

Figures 19 and 20 show, in case of LYSO and Pb-Scint respectively, the anti-neutron-IS photon missing mass for different values of M_{had} .

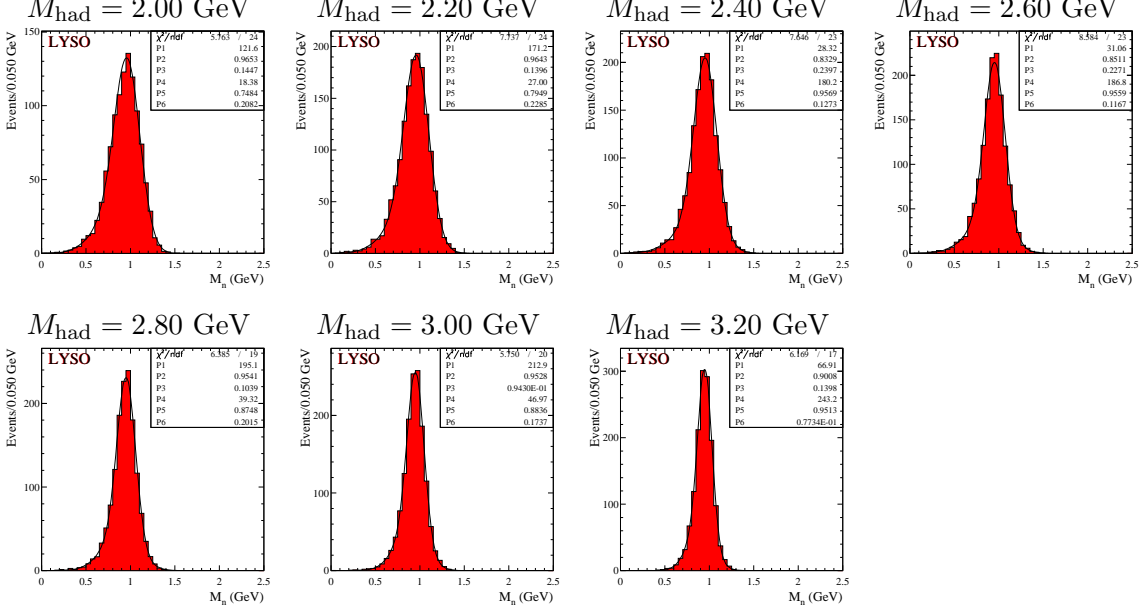


Figure 19: Anti-neutron-IS photon missing mass distributions obtained in the case of LYSO detector for seven energies. The curves are the fits.

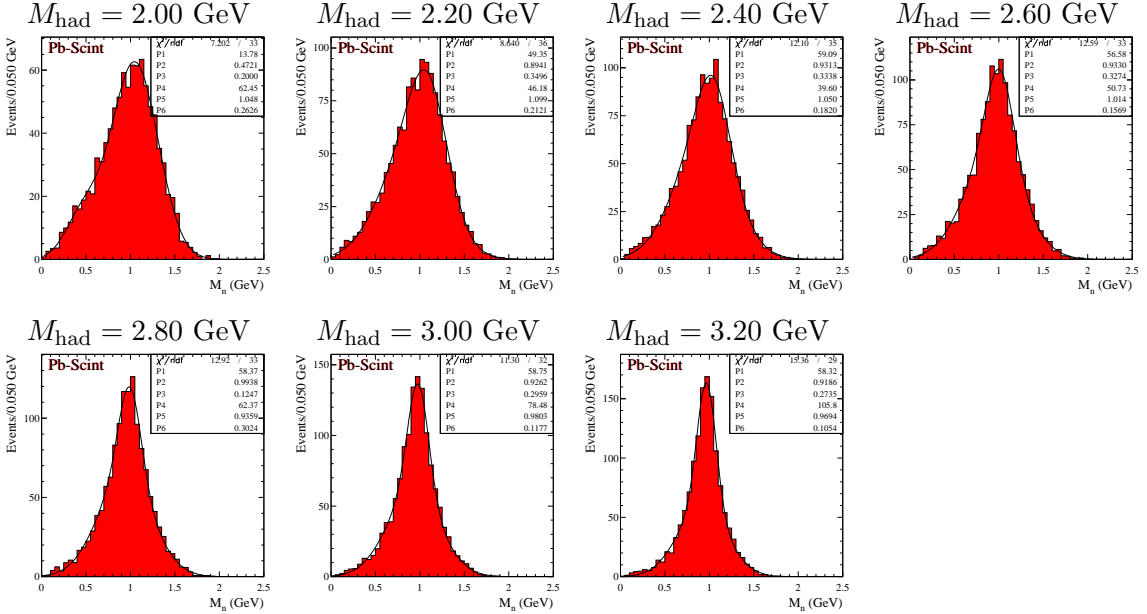


Figure 20: Anti-neutron-IS photon missing mass distributions obtained in the case of Pb-Scint detector for seven energies. The curves are the fits.

In fig. 21 we report trends of the n width as obtained fitting distributions of figs. 19 and 20 with two gaussians. The plotted quantity σ_n is the half width of the area, symmetric w.r.t.

the center of mass of the distributions, which contains the 68% of events.

In this case the error that dominates is that of the \bar{n} momentum. Indeed we have better resolution at higher M_{had} , i.e. lower photon energies. At this regime, even though the total hadronic momentum must be small, each single baryon can still have a complete spectrum of momenta.

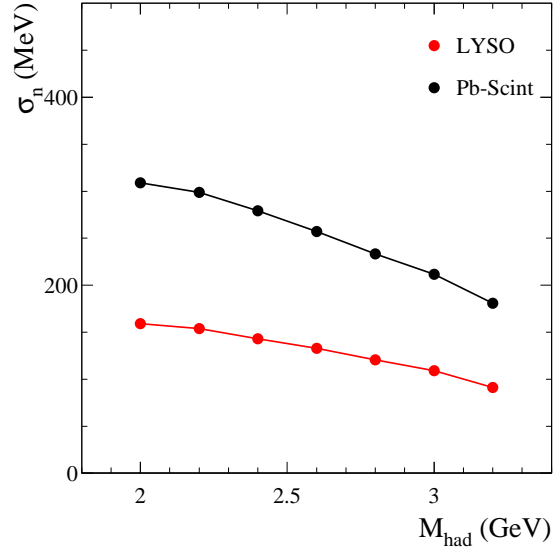


Figure 21: Widths of the $e^+e^-\gamma_{\text{IS}}\bar{n}$ missing mass distributions in case of LYSO (red) and Pb-Scint (black) case.

5. Including π^0

We consider now the contamination due to the production of $n\bar{n}\pi^0\gamma_{\text{IS}}$ final states as described in Sec. 3.2.

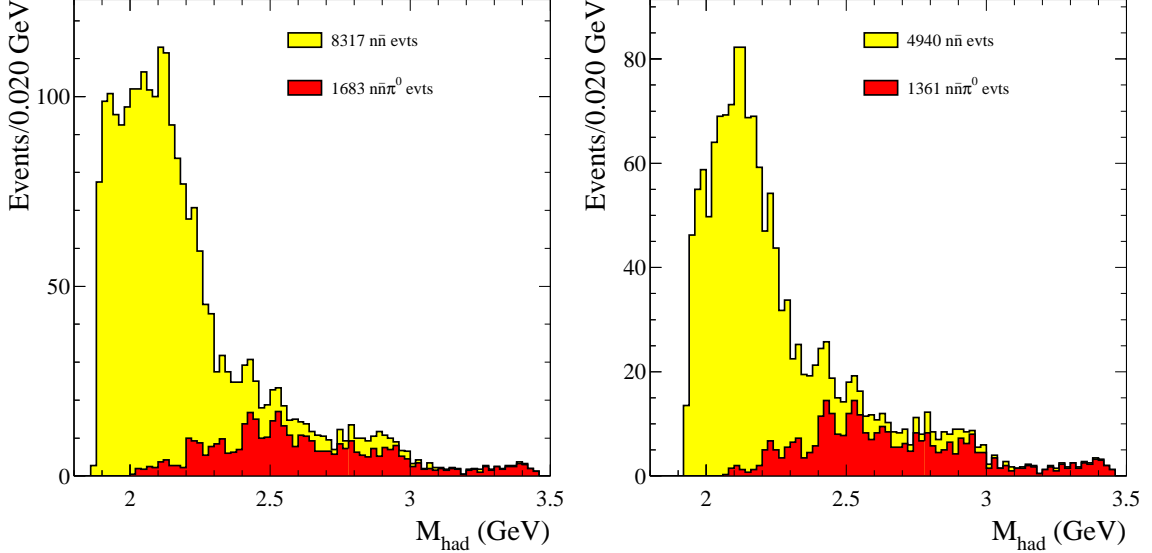


Figure 22: Yields of generated $e^+e^- \rightarrow n\bar{n}\gamma_{\text{IS}}$ events in yellow and $e^+e^- \rightarrow n\bar{n}\pi^0\gamma_{\text{IS}}$ in red before (left) and after (right) the geometrical cut.

Pictures of fig. 22 show the yields of generated events, without any cut on the left, with the geometrical cut on the right. Portions of pure $e^+e^- \rightarrow n\bar{n}\gamma_{\text{IS}}$ and $e^+e^- \rightarrow n\bar{n}\pi^0\gamma_{\text{IS}}$ are indicated by the yellow and red histograms respectively.

Pictures of fig. 23 show yields after the KF and requiring only π^0 that escape detection (see Sec. 3.2), in case of LYSO and Pb-Scint detectors. The amount of π^0 contamination is drastically reduced. Figure 24 shows the two χ^2 's and fig. 25 the effect of the KF- χ^2 cut.

5.1 Energy slices in M_{had}

As before, we consider seven values of M_{had} , the energy of the whole hadronic final state, from 2.0 up to 3.2 GeV in steps of 0.2 GeV. Figures 26 and 27 show the M_{had} energies reconstructed with the KF procedure, in red the pure $n\bar{n}\gamma_{\text{IS}}$ final states, in green $n\bar{n}\pi^0\gamma_{\text{IS}}$. These distributions have been fitted with two gaussians.

Figures 28 and 29 show the energy resolutions and the percentage of events surviving to the geometrical and KF cuts.

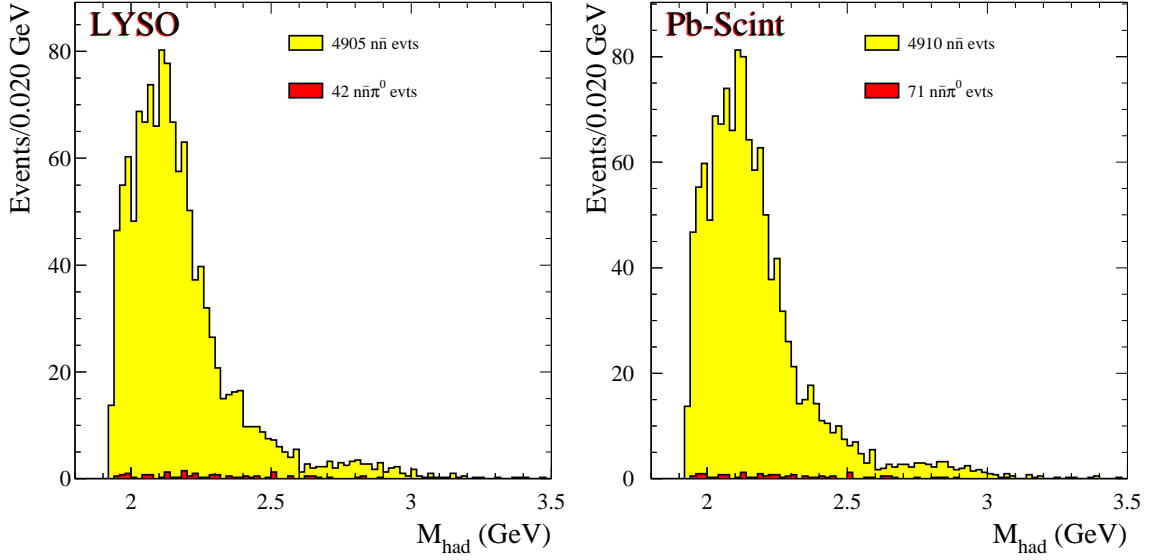


Figure 23: Yields of generated $e^+e^- \rightarrow n\bar{n}\gamma_{\text{IS}}$ events in yellow and $e^+e^- \rightarrow n\bar{n}\pi^0\gamma_{\text{IS}}$ in red before (left) and after (right) the KF.

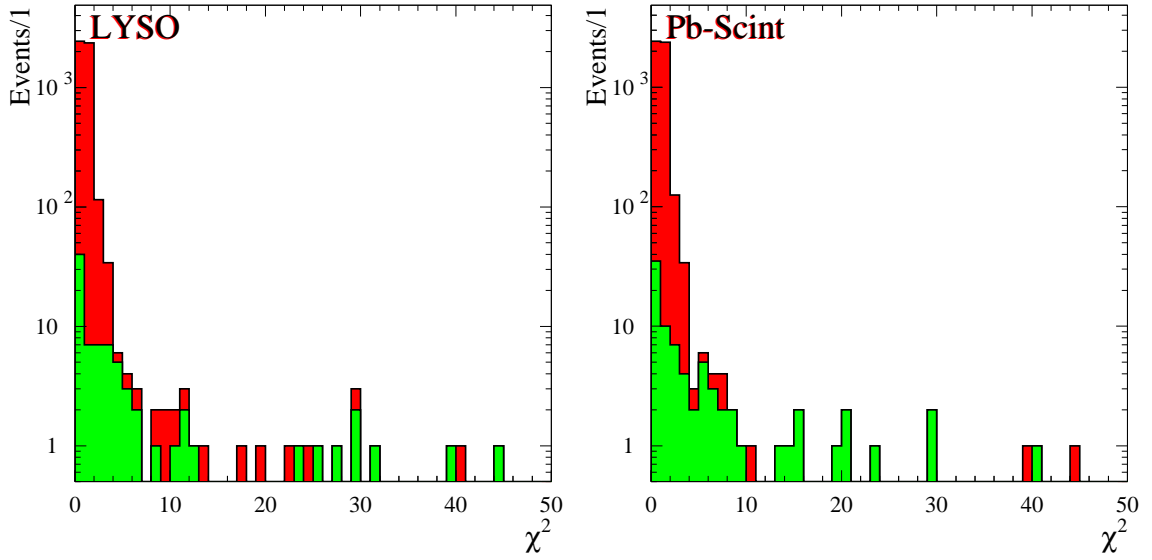


Figure 24: χ^2 distribution for $e^+e^- \rightarrow n\bar{n}\gamma_{\text{IS}}$ (red) and $e^+e^- \rightarrow n\bar{n}\pi^0\gamma_{\text{IS}}$ (green) events, where only γ_{IS} and \bar{n} are detected. LYSO on the left and Pb-Scint on the right.

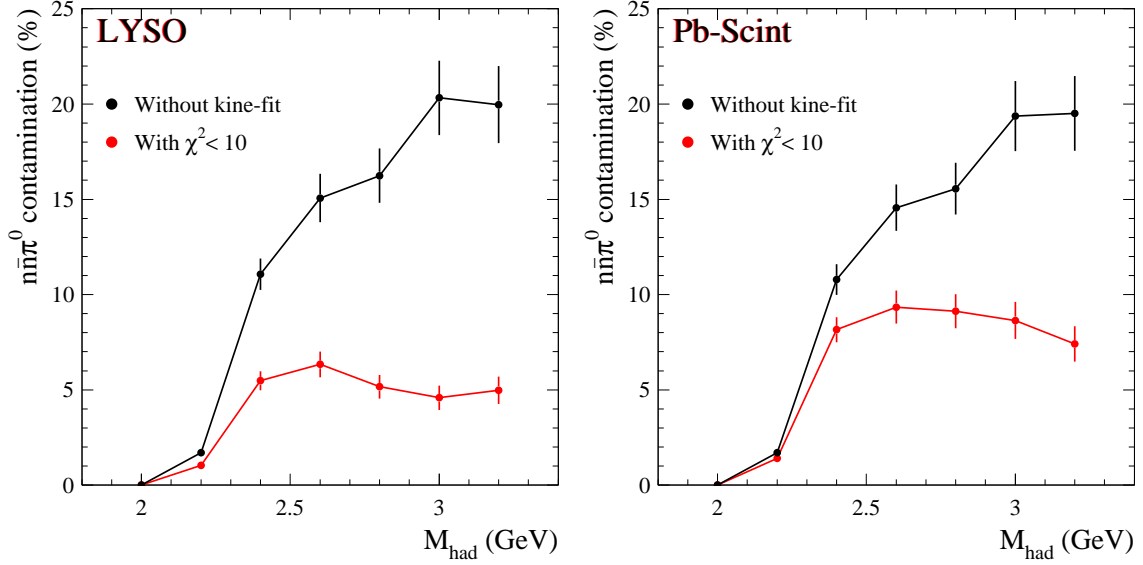


Figure 25: Percentage of π^0 background events before (black) and after (red) the cut on the KF- χ^2 . LYSO on the left and Pb-Scint on the right.

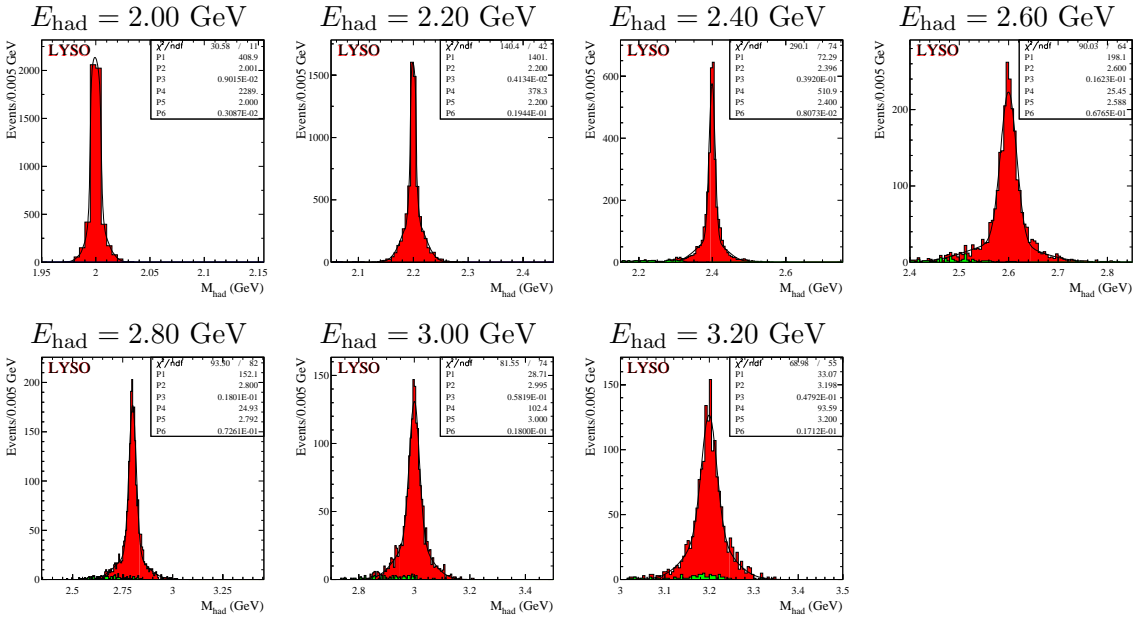


Figure 26: Energy distributions obtained in the case of LYSO detector. Red and green histograms identify pure $\bar{n}\bar{n}\gamma_{1S}$ and $\bar{n}\bar{n}\pi^0\gamma_{1S}$ contributions respectively. Black curves are the fits.

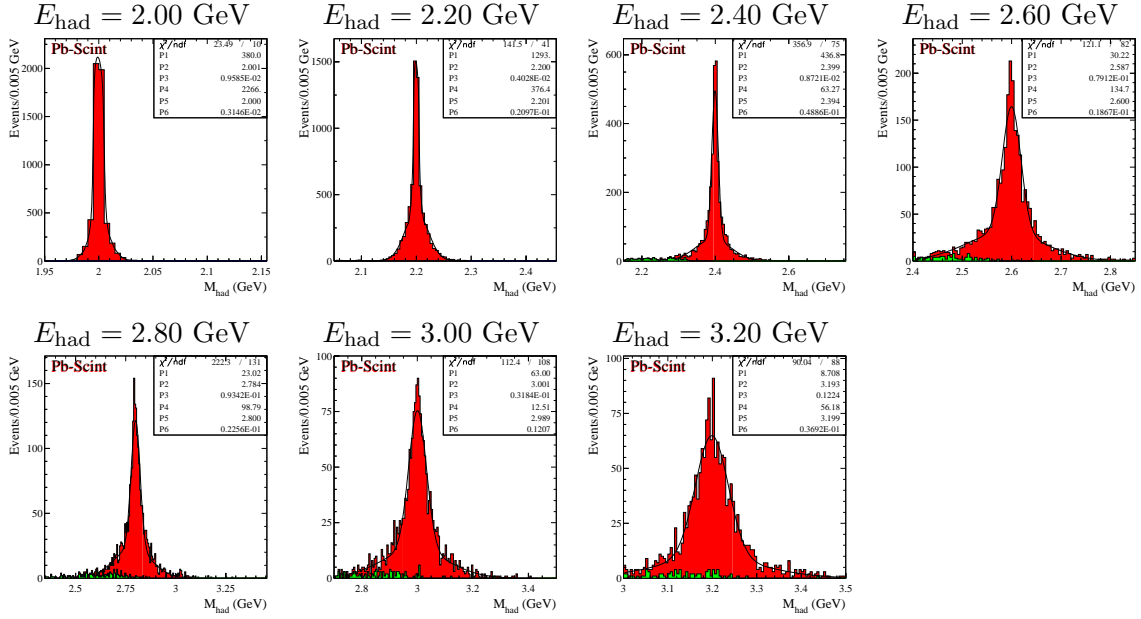


Figure 27: Energy distributions obtained in the case of Pb-Scint detector. Red and green histograms identify pure $n\bar{n}\gamma_{\text{IS}}$ and $n\bar{n}\pi^0\gamma_{\text{IS}}$ contributions respectively. Black curves are the fits.

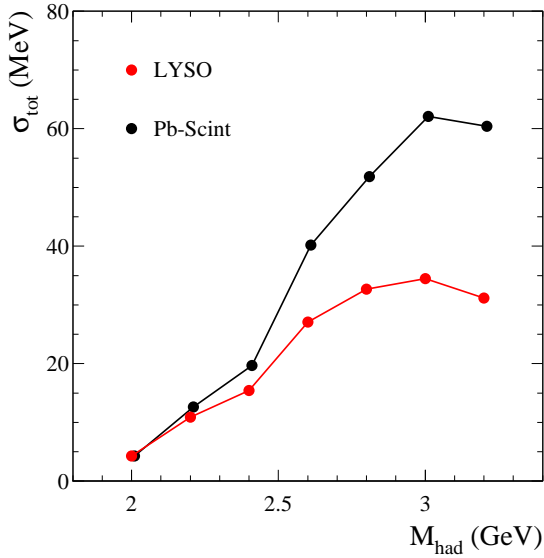


Figure 28: Energy resolution in the hadronic invariant mass for the LYSO (red) and Pb-Scint (black) case.

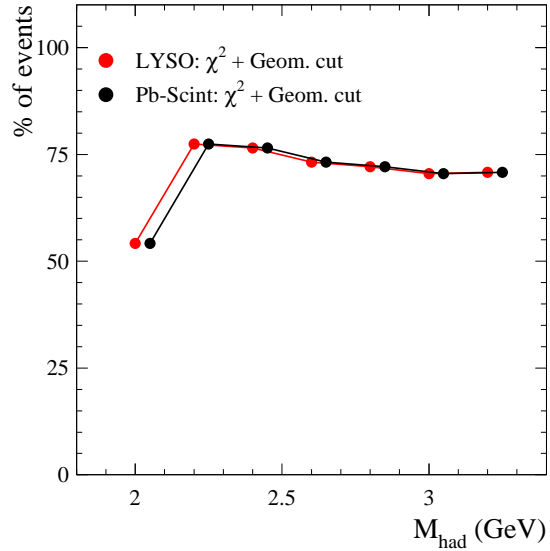


Figure 29: Percentage of events surviving to the geometrical cut, π^0 not detected and $\text{KF-}\chi^2 < 10$.

5.2 The $\bar{n}\gamma_{\text{IS}}$ missing mass with π^0 contamination

Figure 30 and 31 show, in case of LYSO and Pb-Scint respectively, the anti-neutron-IS photon missing mass for different values of M_{had} .

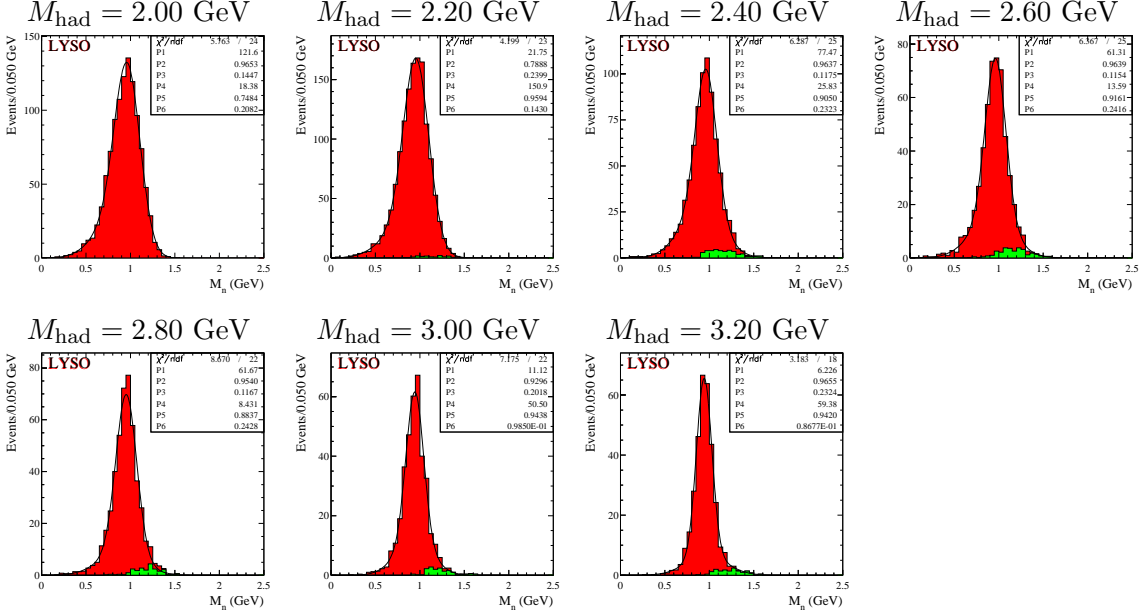


Figure 30: Anti-neutron-IS photon missing mass distributions obtained in the case of LYSO detector for seven energies. Red and green histograms stand for pure $n\bar{n}$ and $n\bar{n}\pi^0$ contributions. The curves are the fits.

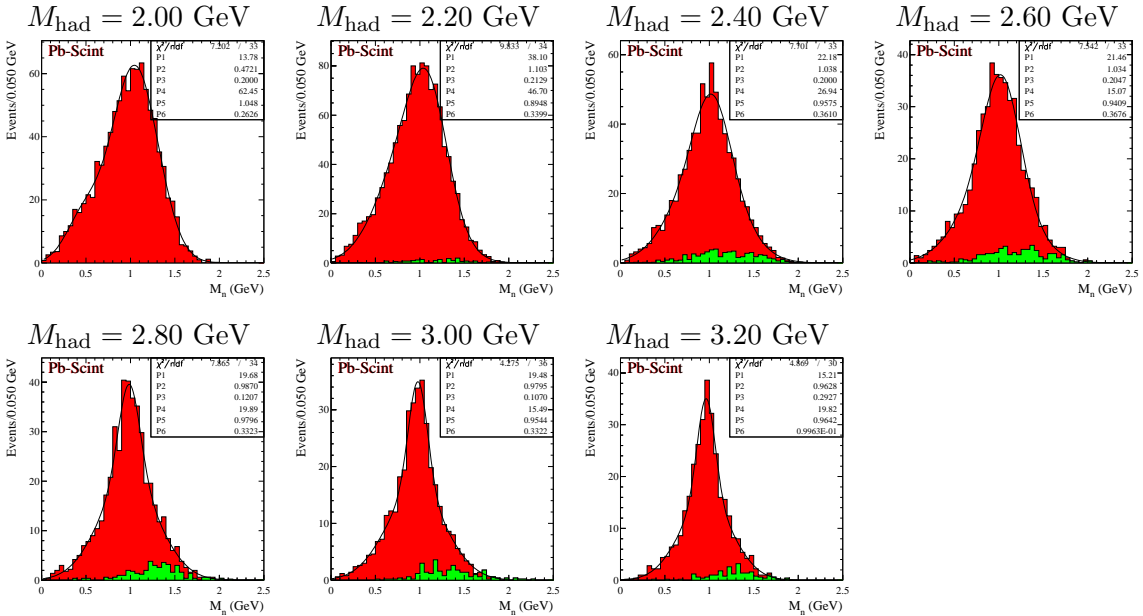


Figure 31: Anti-neutron-IS photon missing mass distributions obtained in the case of Pb-Scint detector for seven energies. Red and green histograms stand for pure $n\bar{n}$ and $n\bar{n}\pi^0$ contributions. The curves are the fits.

In fig. 32 we report trends of the n width as obtained fitting distributions of figs. 30 and 31 with two gaussians and using the procedure described in Sec. 4.2.

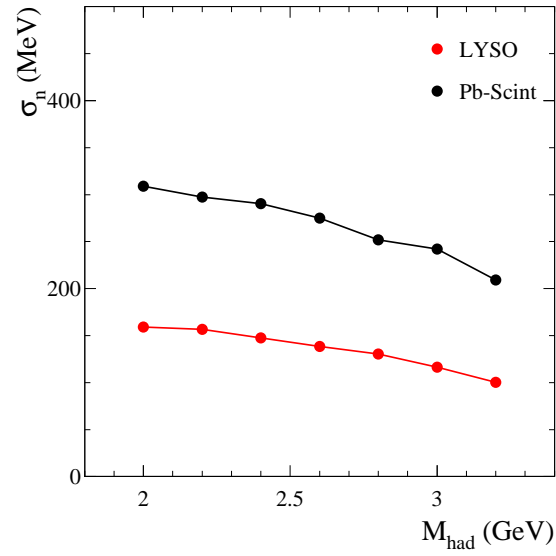


Figure 32: Widths of the $e^+e^-\gamma_{\text{IS}}\bar{n}$ missing mass distributions in case of LYSO (red) and Pb-Scint (black) case.

6. Radiation hardness

We compute the dose D absorbed by the ZDD during one year of data taking. It corresponds to the energy imparted by ionizing radiation in a volume element of a specified material divided by its mass. This quantity is expressed in units of gray (Gy) or rad that have dimensions of an energy divided by a mass. More in detail [8]

$$1 \text{ Gy} = 1 \text{ J/kg} = 100 \text{ rad} = 6.24 \times 10^{18} \text{ eV/kg} \quad (6.1)$$

$$1 \text{ rad} = 6.24 \times 10^{16} \text{ eV/kg} \quad \Rightarrow \quad 1 \text{ eV/kg} = 1.6 \times 10^{-17} \text{ rad}.$$

It follows that, considering a single ZDD element, one fourth of its total surface, the absorbed dose can be written as

$$D = \frac{E_{\text{ZDD}/4}^{\gamma}}{M_{\text{ZDD}/4}} = \frac{N_{\text{ZDD}/4}^{\gamma} \cdot E_{\text{mean}}}{M_{\text{ZDD}/4}}, \quad (6.2)$$

where $N_{\text{ZDD}/4}^{\gamma}$ represents the number of photons that hit a ZDD element in one year ($T = 1.5 \times 10^7$ s) of data taking, E_{mean} is their mean energy, hence $E_{\text{ZDD}/4}^{\gamma}$ is the corresponding deposited energy. The number of photons can be obtained using the ZDD Bremsstrahlung cross section given in eq. (1.1) and the average value of the luminosity: $\bar{\mathcal{L}} = 1.5 \times 10^{32} \text{ cm}^{-2}\text{s}^{-1}$, it reads

$$\begin{aligned} N_{\text{ZDD}/4}^{\gamma} &= \sigma(\text{ZDD})/4 \cdot \bar{\mathcal{L}} \cdot T \\ &= 2.6 \text{ mb} \cdot 1.5 \times 10^{32} \text{ cm}^{-2}\text{s}^{-1} \cdot 1.5 \times 10^7 \text{ s} \\ &= 2.6 \times 10^{-27} \text{ cm}^{-2} \cdot 1.5 \times 10^{32} \text{ cm}^{-2}\text{s}^{-1} \cdot 1.5 \times 10^7 \text{ s} \\ &= 5.9 \times 10^{12}. \end{aligned} \quad (6.3)$$

Assuming an energy distribution which scales as the $1/E$, the average energy over the interval $[E_{\text{min}}, E_{\text{max}}] = [0.050 \text{ GeV}, 1.87 \text{ GeV}]$ is

$$E_{\text{mean}} = \frac{E_{\text{max}} - E_{\text{min}}}{\ln(E_{\text{max}}/E_{\text{min}})} = \frac{1.87 - 0.05}{\ln(1.87/0.05)} \text{ GeV} = 0.5 \text{ GeV}. \quad (6.4)$$

Using results of eqs. (6.3) and (6.4), the Bremsstrahlung energy per year over ZDD/4 is

$$E_{\text{ZDD}/4}^{\gamma} = 5.9 \times 10^{12} \cdot 5 \times 10^8 \text{ eV} = 3 \times 10^{21} \text{ eV}. \quad (6.5)$$

In both cases, LYSO and Pb-Scint detectors, the volume in which the photons dissipate their energy is $1 \times 1 \times 16 \text{ cm}^3$. But while in case of LYSO the whole volume is “active”, in case of Pb-Scint, only one half of the volume, the portion represented by scintillating fibers, is active and then subject to radiation damages. The fraction of energy absorbed by the scintillating fiber is $F_{\text{Scint}} = 2/13$, while $F_{\text{LYSO}} = 1$. The densities of the two active materials are $\rho_{\text{LYSO}} = 7.4 \text{ g cm}^{-3}$ and $\rho_{\text{Scint}} = 0.93 \text{ g cm}^{-3}$, then the masses

$$M_{\text{LYSO}} = 16 \text{ cm}^3 \cdot 7.4 \text{ g cm}^{-3} = 0.12 \text{ kg}, \quad (6.6)$$

$$M_{\text{Scint}} = 16 \text{ cm}^3 \cdot 0.93 \text{ g cm}^{-3}/2 = 7.4 \times 10^{-3} \text{ kg},$$

where the factor of 1/2 in case of Scint accounts for the only scintillating fiber volume. Finally, following eq. (6.2), the absorbed doses are

$$D_{\text{LYSO}} = \frac{E_{\text{ZDD}/4}^{\gamma} \cdot F_{\text{LYSO}}}{M_{\text{LYSO}}} = \frac{3 \times 10^{21} \cdot 1}{0.12} \frac{\text{eV}}{\text{kg}} = 2.5 \times 10^{22} \frac{\text{eV}}{\text{kg}} = 4 \times 10^5 \text{ rad},$$

$$D_{\text{Scint}} = \frac{E_{\text{ZDD}/4}^{\gamma} \cdot F_{\text{Pb-Scint}}}{M_{\text{Pb-Scint}}} = \frac{3 \times 10^{21} \cdot 2/13}{1.8 \times 10^{-2}} \frac{\text{eV}}{\text{kg}} = 6.2 \times 10^{22} \frac{\text{eV}}{\text{kg}} = 10^6 \text{ rad},$$
(6.7)

where we have used masses of eq. (6.6) and the conversion “eV/kg \rightarrow rad” defined in eq. (6.1).

References

- [1] S. M. Swanson, Phys. Rev. **154**, 1601 (1967).
- [2] M. Ablikim *et al.* [BESIII Collaboration], arXiv:0911.4960 [physics.ins-det].
- [3] G. Xu, L. Chen, N. Huang, Q. Qin and X. Wen, *Prepared for 8th European Particle Accelerator Conference (EPAC 2002), Paris, France, 3-7 Jun 2002.*
- [4] P. Branchini, F. Ceradini, G. Corradi, B. D. Micco and A. Passeri, J. Phys. Conf. Ser. **160**, 012022 (2009).
- [5] B. Aubert *et al.* [BABAR Collaboration], Phys. Rev. D **73**, 012005 (2006) [arXiv:hep-ex/0512023].
- [6] B. Aubert *et al.* [BABAR Collaboration], Phys. Rev. D **76**, 092006 (2007) [arXiv:0709.1988 [hep-ex]].
- [7] A. Zallo, private communication.
- [8] C. Amsler *et al.* (Particle Data Group), Phys. Lett. B **667**, 1 (2008).